

PAPER

# Phonon excitations in $\text{Eu}_2\text{Ir}_2\text{O}_7$ probed by inelastic x-ray scattering



To cite this article: Han Wang *et al* 2024 *J. Phys.: Condens. Matter* **36** 425705

View the [article online](#) for updates and enhancements.

## You may also like

- [Mapping the structural, magnetic and electronic behavior of  \$\(\text{Eu}\_{1-x}\text{Ca}\_x\)\_2\text{Ir}\_2\text{O}\_7\$  across a metal-insulator transition](#)  
Eli Zoghlin, Zach Porter, Samuel Britner et al.
- [Topological properties and functionalities in oxide thin films and interfaces](#)  
Masaki Uchida and Masashi Kawasaki
- [Selective probing of magnetic order on Tb and Ir sites in stuffed  \$\text{Tb}\_2\text{Ir}\_2\text{O}\_7\$  using resonant x-ray scattering](#)  
C Donnerer, M C Rahn, E Schierle et al.

# Phonon excitations in $\text{Eu}_2\text{Ir}_2\text{O}_7$ probed by inelastic x-ray scattering

Han Wang<sup>1</sup> , Ryoma Kaneko<sup>2,3</sup>, Kentaro Ueda<sup>2,3,\*</sup>, Yang Zhang<sup>4</sup> , Alfred Q R Baron<sup>5</sup> , Daisuke Ishikawa<sup>5</sup>, Björn Wehinger<sup>6</sup> , Elbio Dagotto<sup>4,7</sup>, Yoshinori Tokura<sup>2,3,8</sup>, Taka-hisa Arima<sup>2,9</sup> and Shang Gao<sup>1,2,\*</sup>

<sup>1</sup> Department of Physics, University of Science and Technology of China, Hefei 230026, People's Republic of China

<sup>2</sup> RIKEN Center for Emergent Matter Science, Wako 351-0198, Japan

<sup>3</sup> Department of Applied Physics, University of Tokyo, Tokyo 113-8656, Japan

<sup>4</sup> Department of Physics and Astronomy, University of Tennessee, Knoxville, TN 37996, United States of America

<sup>5</sup> Materials Dynamics Laboratory, RIKEN SPring-8 Center, Sayo 679-5198, Japan

<sup>6</sup> European Synchrotron Radiation Facility, 71, Avenue des Martyrs, Grenoble 38000, France

<sup>7</sup> Materials Science and Technology Division, Oak Ridge National Laboratory, TN 37831, United States of America

<sup>8</sup> Tokyo College, University of Tokyo, Tokyo 113-8656, Japan

<sup>9</sup> Department of Advanced Materials Science, University of Tokyo, Kashiwa 277-8561, Japan

E-mail: [ueda@ap.t.u-tokyo.ac.jp](mailto:ueda@ap.t.u-tokyo.ac.jp) and [sgao@ustc.edu.cn](mailto:sgao@ustc.edu.cn)

Received 12 May 2024, revised 25 June 2024

Accepted for publication 8 July 2024

Published 23 July 2024



## Abstract

The study of phonon dynamics and its interplay with magnetic ordering is crucial for understanding the unique quantum phases in the pyrochlore iridates. Here, through inelastic x-ray scattering on a single crystal sample of the pyrochlore iridate  $\text{Eu}_2\text{Ir}_2\text{O}_7$ , we map out the phonon excitation spectra in  $\text{Eu}_2\text{Ir}_2\text{O}_7$  and compare them with the theoretical phonon spectra calculated using the density functional theory. Possible phonon renormalization across the magnetic long-range order transition is observed in our experiments, which is consistent with the results of the previous Raman scattering experiments.

Keywords: spin–orbit coupling (SOC), phonon excitations, inelastic x-ray scattering (IXS), density functional theory

## 1. Introduction

The explorations of the  $4d$  and  $5d$  heavy transitional metal electronic systems represent a cutting-edge research domain in condensed matter physics. Due to a unique amalgamation of extended  $5d/4d$  orbitals [1], strong spin–orbit coupling (SOC), and geometrically frustrated lattices [2], this family of heavy transitional metal materials offers a rich platform to search for exotic correlated states. Till now, a plethora of novel phases have been discovered in the  $4d$ - and  $5d$ -based materials, including quantum spin liquids [3–5], metal–insulator

transitions [6, 7], Weyl semimetals [8], topological insulators [9, 10], non-Fermi liquids [11], magnetic monopole-like phase [12].

Among the heavy transitional metal electronic systems, the pyrochlore iridates,  $R_2\text{Ir}_2\text{O}_7$  ( $R = \text{Y}$  and rare earth ions) [13–18], have drawn great interests. The structure of the pyrochlore iridates is presented in figure 1(a), where the  $\text{Ir}^{4+}$  ions form a pyrochlore lattice with corner-sharing tetrahedra. The  $\text{Ir}^{4+}$  ions of the low-spin configuration form an effective doublet of  $J = 1/2$ , where  $J$  is the total angular momentum [19]. For compounds with a relatively large  $R^{3+}$  ion radius, a metal–insulator transition (MIT) has been observed, where the transition temperature,  $T_N$ , can be tuned by various external parameters including chemical composition [20–22],

\* Authors to whom any correspondence should be addressed.

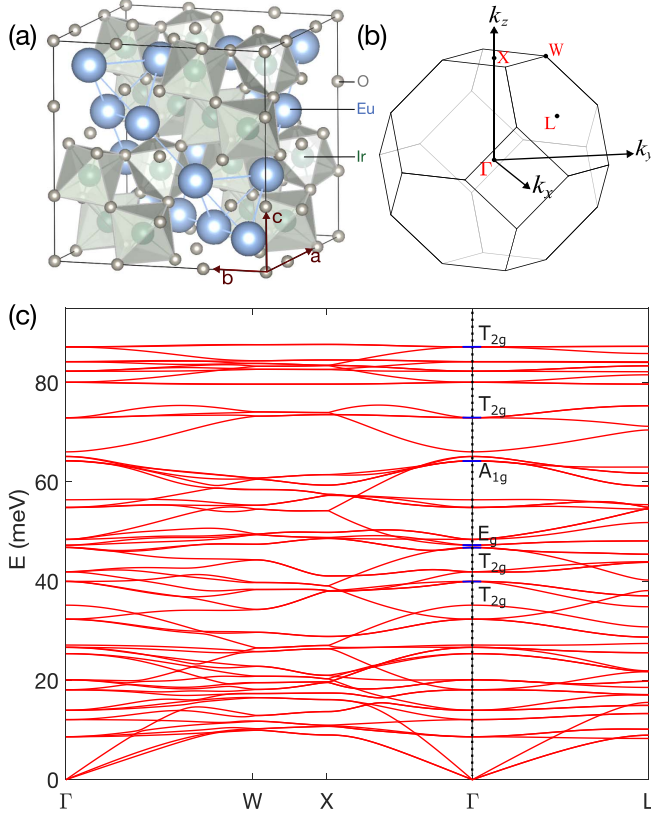


**Figure 1.** (a) Crystal structure of the pyrochlore iridates. The large blue sphere is the Eu site. The large green sphere inside the polyhedra is Ir. The small grey sphere is O. (b) The first Brillouin zone and high symmetry points of the face-centered cubic (FCC) lattice. (c) DFT calculations of the phonon dispersion along the high-symmetry directions  $\Gamma$ -W-X- $\Gamma$ -L.

pressure [23–25], and magnetic field [26–29]. In the insulating phase, the magnetic moments of the  $\text{Ir}^{4+}$  ions form an ‘all-in/all-out’ (AIAO) magnetic long range-order, which can be viewed as a solidified phase of magnetic monopoles [30]. For compounds with a relatively small  $R^{3+}$  ion radius, the paramagnetic phase at temperatures above the ordering transition become insulating, indicating a strong correlation between the chemical pressure and electronic bands [31].

The lattice degree of freedom of the pyrochlore iridates also contains rich information about the spin correlations because the lattice is directly connected to the orbitals and, consequently, indirectly influences the spins through SOC [32, 33]. Recent Raman scattering experiments on  $\text{Eu}_2\text{Ir}_2\text{O}_7$  and the related compounds revealed significant renormalization of the phonon frequencies together with the emergence of magnon modes below the magnetic transition temperature,  $T_N$  [18, 34]. As the noncollinear character of the AIAO structure allows a linear coupling between the magnons and phonons, hybridized spin-lattice excitations may emerge if the magnetoelastic coupling is strong [35].

In this work, we performed non-resonant inelastic x-ray scattering (IXS) experiments to map out the phonon dispersion in  $\text{Eu}_2\text{Ir}_2\text{O}_7$  and compare it to the theoretical spectra calculated by the first-principle density functional theory (DFT).

Possible phonon renormalization across  $T_N$  is observed at selected wave vector transfers near the Brillouin zone center, although hybrid magnon-phonon excitations are not resolved in our experiments possibly due to their relatively low scattering cross sections.

## 2. Methods

Our IXS experiments were performed on the RIKEN Quantum NanoDynamics Beamline, BL43LXU [36], at the SPring-8 synchrotron light source in Japan. This beamline provides world-leading intensity for IXS experiments using  $3 \times 5$  m insertion devices [37, 38] in a small,  $50 \mu\text{m}$  diameter beam spot. A piece of KF-flux grown  $\text{Eu}_2\text{Ir}_2\text{O}_7$  single crystal [39], with a dimension of  $0.4 \times 0.4 \times 0.1 \text{ mm}^3$ , was used for the experiments. The reflection scattering geometry was employed due to the relatively short attenuation length of  $\sim 20 \mu\text{m}$  at an incoming x-ray energy of 20 keV. The (111) surface of the crystal was polished and vertically attached to the sample holder, which was then aligned with the (HKL) plane horizontally. The 24 analyzer array allows parallel measurements over a large area of momentum transfers. The Si (11,11,11) setup with a resolution of  $\gtrsim 1.3 \text{ meV}$  (depending on analyzer) was employed. A closed cycle cryostat was mounted in the Eulerian cradle to access temperatures down to  $\sim 50 \text{ K}$ . The IXS energy scale is expected to be accurate to 0.5 % based on calibration against a standard [40].

Theoretical phonon spectra for  $\text{Eu}_2\text{Ir}_2\text{O}_7$  at zero temperature were calculated using the first-principles DFT as implemented in the Vienna *ab initio* simulation package (VASP). The projector augmented wave method with the generalized gradient approximation and the Perdew–Burke–Ernzerhof exchange potentials were employed [41–44]. The Debye Waller factor was not considered in our calculations. The plane-wave cutoff energy was set as 600 eV and the  $k$ -point mesh was set as  $6 \times 6 \times 6$  for the conventional cell of the cubic  $Fd\bar{3}m$  phase (No. 227) of  $\text{Eu}_2\text{Ir}_2\text{O}_7$ . For the structural optimization in the paramagnetic phase, the lattice constant was fixed at the experimental value of  $a = 10.167 \text{ \AA}$ , and the atomic positions were fully relaxed until the Hellman–Feynman force on each atom was smaller than  $0.001 \text{ eV \AA}^{-1}$ . Following the previous study [34], our phonon calculations do not consider the magnetic order. Force constants were calculated by density functional perturbation theory [45, 46] as implemented in VASP. Phonon dispersion relations were obtained using the PHONOPY software in a primitive unit cell [47, 48].

## 3. Results and discussions

Figure 1 presents an overview of the calculated phonon dispersion along the high symmetry lines in reciprocal space. The absence of imaginary frequencies corroborates the accuracy of our structural optimization. Altogether 66 phonon bands are observed in our calculations, which is consistent with the number of phonon modes for 22 atoms per primary unit cell. At the Brillouin zone center, i.e. the  $\Gamma$  point, there are

**Table 1.** Comparison between the experimentally determined and calculated energies of the Raman-active phonon modes for  $\text{Eu}_2\text{Ir}_2\text{O}_7$  at room temperature. Energies are measured in units of meV.

	$T_{2g}(1)$	$E_g$	$T_{2g}(2)$	$A_{1g}$	$T_{2g}(3)$	$T_{2g}(4)$
experimental [34]	37.5	41.8	47.1	63.0	67.3	84.3
previous cal. [34]	39.3	46.0	51.7	65.7	72.9	83.9
our DFT cal.	39.9	47.2	48.4	66.1	72.9	87.2

**Table 2.** Comparison between the experimentally determined and calculated energies of the infrared-active  $T_{1u}$  phonon modes  $\text{Eu}_2\text{Ir}_2\text{O}_7$  at room temperature. Energies are measured in units of meV.

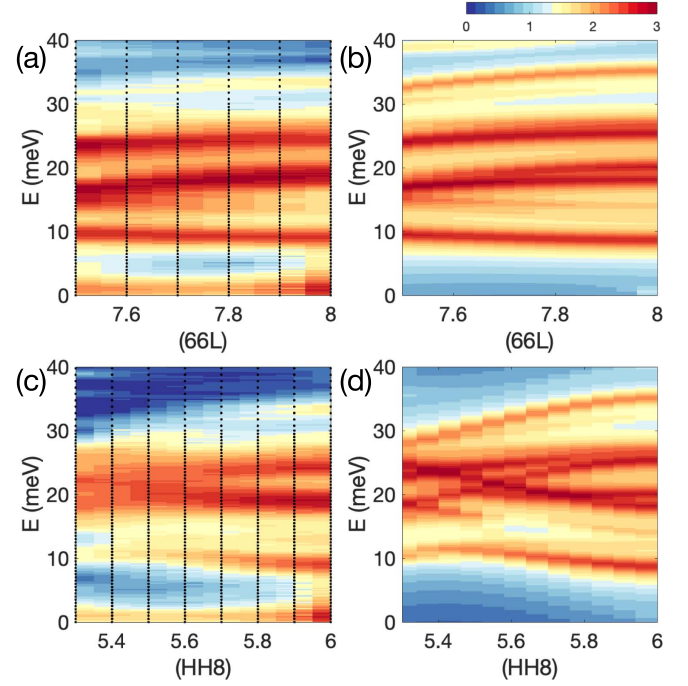
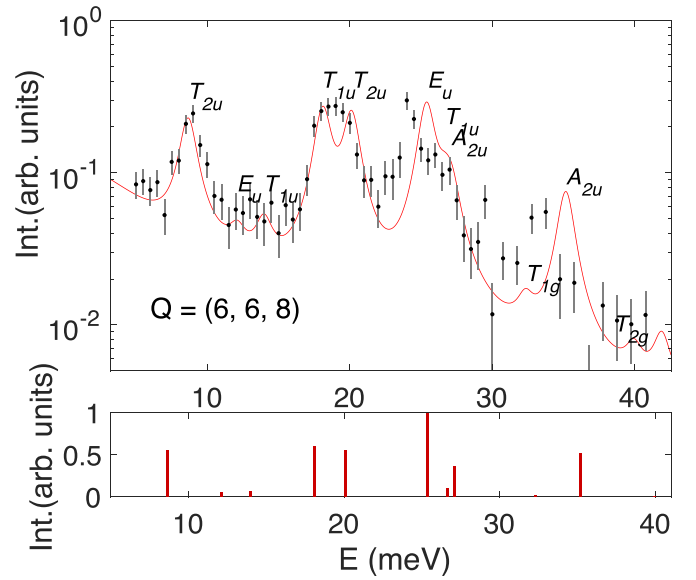
	$T_{2u}$	$E_u$	$T_{1u}$	$A_{1u}$	$T_{2u}$	$T_{1u}$	$A_{2u}$
experimental [34]	14.2	18.5	25.6	42.1	53.8	60.5	78.5
previous cal. [34]	13.9	18.6	27.3	45.4	57.2	61.6	77.6
our DFT cal.	14.0	18.1	26.6	41.9	54.8	64.2	80.0

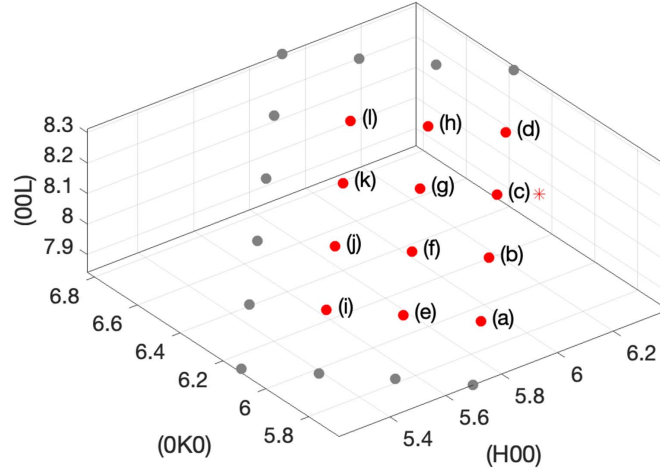
6 Raman-active phonon bands according to group-theoretical analysis [34],

$$\Gamma^{\text{op}} = A_{1g} + E_g + 4T_{2g}. \quad (1)$$

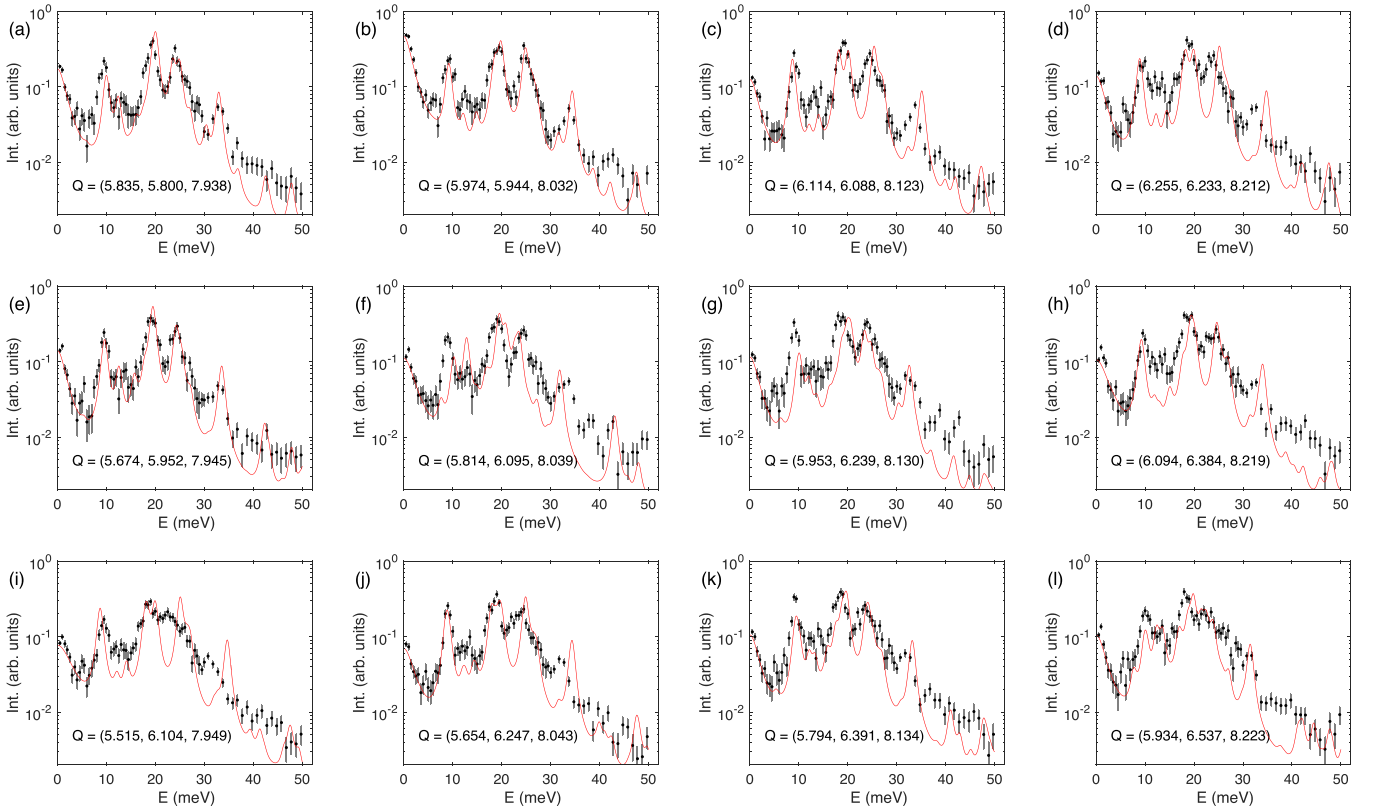
These Raman active modes are indicated in figure 1(c). As compared in tables 1 and 2 for the Raman- and infrared-active modes, respectively, our calculated frequencies are in good agreement with the previous DFT calculations and the experimental observations at  $T = 300$  K [34]. For the  $E_g$  mode that is the focus of our present study, the calculated and experimental energies are 47.2 and 41.8 meV, respectively. This slightly overestimated energy may arise from the coupling between phonons and low-energy excitations of the valence electrons [34], which is not included in DFT calculations.

Figure 2 compares the experimental and calculated IXS cross sections along the (66L) and (HH8) directions around (668) r.l.u. in reciprocal space, with r.l.u. representing the reciprocal lattice unit. This area was selected for our IXS measurements due to the relatively low scattering intensity of the Bragg peak and acoustic phonon modes. The calculated spectra include convolutions with a pseudo-Voigt function with a full width at half maximum matching that measured from plexiglass from the same analyzer with the same momentum acceptance. While more correctly one should use the full resolution function (e.g. as determined by the method of [49]), the pseudo-Voigt approximation was considered sufficient for the present work. A comparison between the experimental and calculated cross sections at (668) r.l.u. up to  $\sim 40$  meV is shown in figure 3, where the red line is the calculated cross section plus a pseudo-Voigt peak at  $E = 0$ . The observed phonon modes at the Brillouin zone center can be identified as the  $T_{2u}$  (8.64),  $E_u$  (12.08),  $T_{1u}$  (13.94),  $T_{1u}$  (18.12),  $T_{2u}$  (20.10),  $E_u$  (25.40),  $T_{1u}$  (26.64),  $A_{2u}$  (27.13),  $T_{1g}$  (32.34),  $A_{2u}$  (35.16), and  $T_{2g}$  (39.95) modes, where the calculated energies in units of meV are shown in brackets following each mode. The dispersion of the phonon excitations, together with their IXS cross sections, are well described by our DFT calculations.

**Figure 2.** (a) Experimental and (b) calculated phonon IXS spectra along the (66L) direction. The experimental data are collected at  $T = 50$  K. (c) Experimental and (d) calculated IXS spectra along the (HH8) direction. The black dots in panels (a) and (c) indicate the positions where IXS spectra were collected. The same colorbar is employed for all panels.**Figure 3.** Experimental (black dots) and calculated (red line) phonon spectra at momentum transfer  $Q = (6, 6, 8)$  measured at  $T = 50$  K. The calculated IXS cross section is convoluted by a pseudo-Voigt instrumental resolution function. The scattering intensity is shown in arbitrary units (a. u.). The phonon modes corresponding to each peak are indicated, with their calculated energy shown by vertical bars at the bottom. The height of the vertical bars corresponds to the calculated IXS cross sections normalized by the cross section of the  $E_u$  mode at  $E = 25.4$  meV.



**Figure 4.** The simultaneously detected 24  $Q$  points in reciprocal space with the targeting detector fixed at  $Q = (6.114, 6.088, 8.123)$  r.l.u. as indicated by the asterisk. Red dots correspond to the selected 12 positions that are presented in figures 5 and 6.



**Figure 5.** Representative IXS spectra of  $\text{Eu}_2\text{Ir}_2\text{O}_7$  measured at  $T = 50$  K with the target detector fixed at  $Q = (6.114, 6.088, 8.123)$  r.l.u. Solid red lines represent the calculated phonon cross section convoluted by a pseudo-Voigt instrumental resolution function.

As the detector bank of the IXS spectrometer at the BL43LXU beamline is composed of 24 detectors that are arranged in a 4-by-6 array, a series of IXS spectra can be collected simultaneously at  $Q$  positions around the target wavevector transfer. For a target wavevector transfer of  $Q = (6.114, 6.088, 8.123)$  r.l.u., the simultaneously detected  $Q$  positions are plotted in figure 4, where the target wavevector position is marked by an asterisk.

Figure 5 presents the IXS spectra collected at 12 representative  $Q$  positions around  $(6, 6, 8)$  r.l.u. measured at  $T = 50$  K, below  $T_N \sim 115$  K. The  $Q$  position for each panel is indicated in figure 4 as red dots. The red lines in figure 5 represent the calculated cross-sections plus a pseudo-Voigt peak with a FWHM of 1.3 meV at  $E = 0$ . The experimental data shown in figure 5 reveals that in the magnetically ordered phase, the strongest IXS cross section is observed in an energy



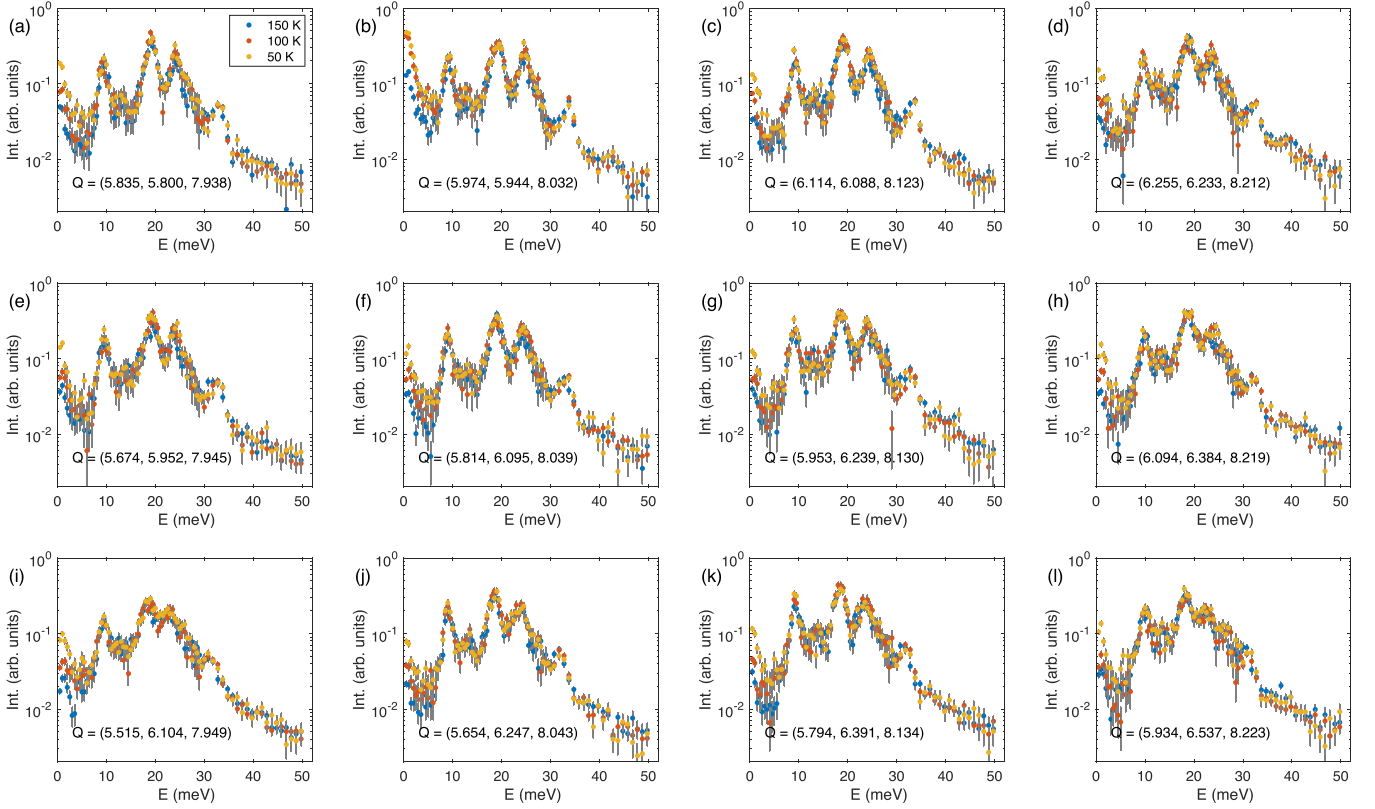


**Figure 6.** Temperature-dependence of the IXS spectra for  $\text{Eu}_2\text{Ir}_2\text{O}_7$  measured at  $T = 50$  K,  $100$  K, and  $150$  K.

transfer range of  $E \sim [10, 30]$  meV, above which the scattering intensity decreases by an order of magnitude up to  $E = 50$  meV. The calculated spectra reproduce the main features of the experimental data, although deviations of  $\sim 2$  meV are observed for the strong modes at 25 and 33 meV. These deviations appear in all detector banks and may be ascribed to the difference in lattice constants employed in our DFT calculations.

Figure 6 compares the IXS spectra for the same 12  $Q$  positions at  $T = 50$ ,  $100$ , and  $150$  K after the thermal factor correction. No strong variation is observed for the main phonon modes in the energy range of  $[10, 30]$  meV, which confirms the absence of structural distortion at  $T_N \sim 115$  K as revealed in the neutron and x-ray diffraction experiments [16, 50, 51]. Focusing at  $Q = (6.114, 6.088, 8.123)$  r.l.u., for which the IXS data in the energy range of  $[15, 30]$  meV and  $[30, 50]$  meV is reproduced in figure 7 in linear scale, the weak peak observed at  $E = 38.8$  meV at  $T = 50$  K gradually shifts to  $E = 42.8$  meV at  $T = 150$  K, leading to a double peak feature at  $T = 100$  K. By fitting the IXS spectra at  $Q = (5.974, 5.944, 8.032)$ ,  $(6.114, 6.088, 8.123)$ , and  $(5.814, 6.095, 8.039)$  r.l.u. at  $T = 150$  K, the energy of this weak mode is interpolated to be 41.8 meV at the  $\Gamma$  point, which agrees well with the energy of the  $E_g$  mode observed at similar temperatures in the previous Raman scattering experiments [34]. Therefore, we can ascribe the energy shift of the weak peak to the renormalization of the  $E_g$  mode. Considering its rather weak intensity, further IXS experiments

with better statistics will be required to resolve the dispersion of the  $E_g$  mode as a function of momentum transfer and temperature.

As proposed in the previous studies [18, 34], the renormalization of the  $E_g$  mode, together with its relatively broad width, can be explained by the magnetoelastic effect. In this scenario, the development of a magnetic long-range order at  $T_N \sim 115$  K affects the vibrations of the magnetic ions and therefore modulates the energy of the phonon excitations. According to the Raman scattering experiments [18, 34], a magnon mode at  $\sim 26$  meV appears at temperatures below  $T_N$ , which may also cause a softening of the  $E_g$  phonon mode through the magnon-phonon hybridization as a consequence of the magnetoelastic effect in the dynamical regime. The distribution in the magnitude of the ordered moment, the size of the magnetic domains, or even the lifetime of the magnon excitations, will induce a variance in the energy shift of the  $E_g$  mode, thus explaining its relative broad width. When the magnetoelastic coupling is strong enough, the magnon mode at  $\sim 26$  meV may possess a sizable phonon component that can be directly detected in IXS experiments [35]. Following this scenario, we searched for emergent hybridized spin-lattice excitations around  $E \sim 26$  meV in our IXS spectra. However, as this energy range overlaps with the strong conventional phonon modes, it is difficult to confirm the existence of the hybridized spin-lattice excitations using our current IXS data.

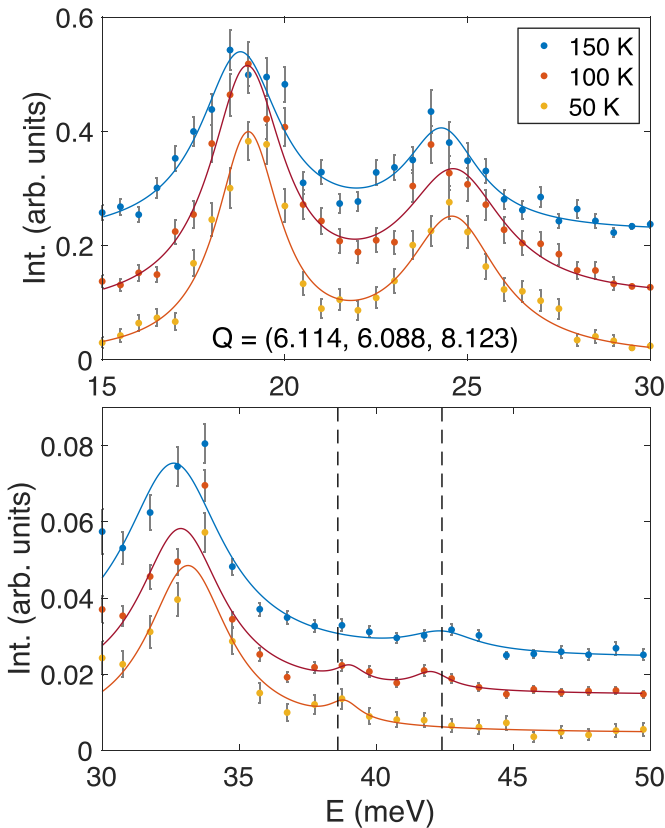


**Figure 7.** Comparison of the IXS spectra for  $\text{Eu}_2\text{Ir}_2\text{O}_7$  at  $Q = (6.114, 6.088, 8.123)$  r.l.u. measured at  $T = 150$  (blue), 100 (red) and 50 K (yellow) in the energy ranges of (a) 15–30 meV and (b) 30–50 meV. Solid lines represent fits to the Lorentzian functions and are guide to the eyes. For clarity, the 100 and 150 K data are shifted along the y axis by 0.1 and 0.2 a. u. respectively in panel (a), and by 0.01 and 0.02 a. u. respectively in panel (b). The dashed lines at 42.4 and 38.6 meV correspond to the positions of the  $E_g$  mode observed in Raman scattering at  $T = 160$  and  $T = 60$  K, respectively.

#### 4. Conclusion

In conclusion, phonon excitations of the pyrochlore iridate  $\text{Eu}_2\text{Ir}_2\text{O}_7$  have been investigated using the non-resonant IXS technique. Comparisons to the DFT calculations reveal that the cross sections are dominated by the Raman-inactive modes in an energy transfer range of [10, 30] meV. Analysis of the IXS spectra measured at temperatures below and above  $T_N$  reveals possible phonon renormalizations across the long-range-order transition as reported in the previous Raman scattering experiments.

#### Data availability statement

All data that support the findings of this study are included within the article (and any supplementary files).

#### Acknowledgments

Works at the USTC was supported by the National Natural Science foundation of China (NSFC) (Grant No. 12374152). Y

Z, and E D were supported by the U.S. Department of Energy, Office of Science, Basic Energy Sciences, Materials Sciences and Engineering Division.

#### ORCID iDs

Han Wang <https://orcid.org/0009-0009-3380-2599>  
 Yang Zhang <https://orcid.org/0000-0003-3623-5883>  
 Alfred Q R Baron <https://orcid.org/0000-0002-5899-2116>  
 Björn Wehinger <https://orcid.org/0000-0002-7089-595X>

#### References

- [1] Takayama T, Chaloupka J, Smerald A, Khaliullin G and Takagi H 2021 *J. Phys. Soc. Japan* **90** 062001
- [2] Gardner J S, Gingras M J and Greedan J E 2010 *Rev. Mod. Phys.* **82** 53
- [3] Okamoto Y, Nohara M, Aruga-Katori H and Takagi H 2007 *Phys. Rev. Lett.* **99** 137207
- [4] Balents L 2010 *Nature* **464** 199–208
- [5] Broholm C, Cava R, Kivelson S, Nocera D, Norman M and Senthil T 2020 *Science* **367** eaay0668
- [6] Streltsov S V and Khomskii D I 2016 *Proc. Natl Acad. Sci. USA* **113** 10491–6
- [7] Matsuhira K, Wakeshima M, Nakanishi R, Yamada T, Nakamura A, Kawano W, Takagi S and Hinatsu Y 2007 *J. Phys. Soc. Japan* **76** 043706
- [8] Xu S Y et al 2015 *Science* **349** 613–7
- [9] Pesin D and Balents L 2010 *Nat. Phys.* **6** 376–81
- [10] Hasan M Z and Kane C L 2010 *Rev. Mod. Phys.* **82** 3045
- [11] Stewart G 2001 *Rev. Mod. Phys.* **73** 797
- [12] Prando G, Telang P, Wilson S D, Graf M J and Singh S 2020 *Phys. Rev. B* **101** 174435
- [13] Kondo T et al 2015 *Nat. Commun.* **6** 10042
- [14] Lefrançois E, Simonet V, Ballou R, Lhotel E, Hadj-Azzem A, Kodjikian S, Lejay P, Manuel P, Khalyavin D and Chapon L C 2015 *Phys. Rev. Lett.* **114** 247202
- [15] Tomiyasu K, Matsuhira K, Iwasa K, Watahiki M, Takagi S, Wakeshima M, Hinatsu Y, Yokoyama M, Ohoyama K and Yamada K 2012 *J. Phys. Soc. Japan* **81** 034709
- [16] Sagayama H, Uematsu D, Arima T H, Sugimoto K, Ishikawa J, O'farrell E and Nakatsuji S 2013 *Phys. Rev. B* **87** 100403
- [17] Disseler S M 2014 *Phys. Rev. B* **89** 140413
- [18] Nguyen T H et al 2021 *Phys. Rev. Lett.* **127** 267203
- [19] Zhao S, Mackie J, MacLaughlin D, Bernal O, Ishikawa J, Ohta Y and Nakatsuji S 2011 *Phys. Rev. B* **83** 180402
- [20] Matsuhira K, Wakeshima M, Hinatsu Y and Takagi S 2011 *J. Phys. Soc. Japan* **80** 094701
- [21] Ueda K, Fujioka J, Takahashi Y, Suzuki T, Ishiwata S, Taguchi Y and Tokura Y 2012 *Phys. Rev. Lett.* **109** 136402
- [22] Ueda K, Fujioka J and Tokura Y 2016 *Phys. Rev. B* **93** 245120
- [23] Sakata M, Kagayama T, Shimizu K, Matsuhira K, Takagi S, Wakeshima M and Hinatsu Y 2011 *Phys. Rev. B* **83** 041102
- [24] Tafti F, Ishikawa J, McCollam A, Nakatsuji S and Julian S 2012 *Phys. Rev. B* **85** 205104
- [25] Ueda K, Fujioka J, Terakura C and Tokura Y 2015 *Phys. Rev. B* **92** 121110
- [26] Ueda K, Fujioka J, Yang B J, Shiohagi J, Tsukazaki A, Nakamura S, Awaji S, Nagaosa N and Tokura Y 2015 *Phys. Rev. Lett.* **115** 056402
- [27] Tian Z, Kohama Y, Tomita T, Ishizuka H, Hsieh T H, Ishikawa J J, Kindo K, Balents L and Nakatsuji S 2016 *Nat. Phys.* **12** 134–8

- [28] Ueda K, Oh T, Yang B J, Kaneko R, Fujioka J, Nagaosa N and Tokura Y 2017 *Nat. Commun.* **8** 15515
- [29] Ueda K, Kaneko R, Ishizuka H, Fujioka J, Nagaosa N and Tokura Y 2018 *Nat. Commun.* **9** 3032
- [30] Wang Y, Weng H, Fu L and Dai X 2017 *Phys. Rev. Lett.* **119** 187203
- [31] Imada M, Fujimori A and Tokura Y 1998 *Rev. Mod. Phys.* **70** 1039
- [32] Calder S *et al* 2016 *Nat. Commun.* **7** 11651
- [33] Kar A and Elizabeth S 2023 *Phys. Rev. B* **108** 134426
- [34] Ueda K, Kaneko R, Subedi A, Minola M, Kim B, Fujioka J, Tokura Y and Keimer B 2019 *Phys. Rev. B* **100** 115157
- [35] Tóth S, Wehinger B, Rolfs K, Birol T, Stuhr U, Takatsu H, Kimura K, Kimura T, Rønnow H M and Rüegg C 2016 *Nat. Commun.* **7** 13547
- [36] Baron A Q *et al* 2010 *SPRING-8 Inf. Newsl* vol 15 p 14
- [37] Baron A Q 2015 arXiv:1504.01098
- [38] Baron A Q 2016 *High-Resolution Inelastic X-Ray Scattering I: Context, Spectrometers, Samples and Superconductors* (Springer) pp 1643–719
- [39] Millican J N, Macaluso R T, Nakatsuji S, Machida Y, Maeno Y and Chan J Y 2007 *Mater. Res. Bull.* **42** 928–34
- [40] Fukui H, Katsura T, Kuribayashi T, Matsuzaki T, Yoneda A, Ito E, Kudoh Y, Tsutsui S and Baron A Q 2008 *J. Synchrotron Radiat.* **15** 618–23
- [41] Kresse G and Hafner J 1993 *Phys. Rev. B* **47** 558
- [42] Kresse G and Furthmüller J 1996 *Phys. Rev. B* **54** 11169–86
- [43] Blöchl P E 1994 *Phys. Rev. B* **50** 17953–79
- [44] Perdew J P, Burke K and Ernzerhof M 1996 *Phys. Rev. Lett.* **77** 3865
- [45] Baroni S, Giannozzi P and Testa A 1987 *Phys. Rev. Lett.* **58** 1861
- [46] Gonze X 1995 *Phys. Rev. A* **52** 1086
- [47] Chaput L, Togo A, Tanaka I and Hug G 2011 *Phys. Rev. B* **84** 094302
- [48] Togo A and Tanaka I 2015 *Scr. Mater.* **108** 1–5
- [49] Ishikawa D and Baron A Q 2021 *J. Synchrotron Radiat.* **28** 804–11
- [50] Das M *et al* 2022 *Phys. Rev. B* **105** 134421
- [51] Clancy J *et al* 2016 *Phys. Rev. B* **94** 024408